The Influence of Arctic Landfast Ice on Seasonal Modulation of the M₂ Tide

Bij de Vaate, I.; Vasulkar, A.N.; Slobbe, D.C.; Verlaan, M.

Citation (APA)
Bij de Vaate, I., Vasulkar, A. N., Slobbe, D. C., & Verlaan, M. (2021). The Influence of Arctic Landfast Ice on Seasonal Modulation of the M₂ Tide. *Journal of Geophysical Research: Oceans*, *126*(5), 1-16. Article e2020JC016630. https://doi.org/10.1029/2020JC016630

Important note
To cite this publication, please use the final published version (if applicable).
Please check the document version above.

The Influence of Arctic Landfast Ice on Seasonal Modulation of the M$_2$ Tide

I. Bij de Vaate[1] , **A. N. Vasulkar[2]** , **D. C. Slobbe[1]** , and **M. Verlaan[2,3]**

[1]Civil Engineering and Geosciences, Delft University of Technology, Delft, The Netherlands, [2]Delft Institute of Applied Mathematics, Delft University of Technology, Delft, The Netherlands, [3]Deltares, Delft, Netherlands

Abstract Seasonal modulation of the M$_2$ tide has been quantified for the entire Arctic Ocean and connected regional seas, using tidal harmonic analysis of water levels derived from Synthetic Aperture Radar altimetry. Results are compared to numerical simulations that model the effect of two limiting cases of seasonal landfast ice cover on the M$_2$ tide. The largest seasonal modulation (up to 0.25 m) is observed along coastlines and in bays. Locally, the presence of landfast ice decreases amplitudes, but in some cases, the opposite effect was observed further afield. In most of the Arctic, winter months experience a later arrival of the tide, except for Hudson Bay where phase advance is observed. Most of the altimeter-derived seasonal modulation could be explained by the modeled impact of landfast ice. However, particularly in the Hudson Bay system there is a discrepancy between model- and altimeter-derived seasonal modulation. This suggests that other seasonal processes are important. Finally, results suggest that the consequences of variations in Arctic landfast ice are not restricted to the Arctic, but affect tidal water levels on a global scale.

Plain Language Summary Tides are an important force in shaping the Arctic climate and environment. It is known that seasonal changes in Arctic sea ice affect local tides. However, observations of these changes are scarce, and many tide models still treat tides as constant throughout the year. As a first of its kind, our study maps the seasonal variations in the main semi-diurnal tide for the entire Arctic region, based on water levels derived from satellite altimetry. To better understand the relation between observed variations in tides and the seasonal sea ice cycle, two models were run with annual maximum and minimum extents of landfast (immobile) sea ice cover. Observations and simulations both show reduced tidal amplitudes in winter months in most regions where landfast ice is present, but some other regions experience increased tides. Not all of the observed seasonal variation in tides could be explained by the influence of sea ice, indicating that further research is needed, to include other seasonal processes. Our models show that seasonal changes in Arctic sea ice cover can also affect global tides.

1. Introduction

Arctic sea ice is subject to large seasonal variations in extent, thickness and mobility. Most of the Arctic region is covered by sea ice in winter months, with a total area of ~15 million km^2; however, this area declines by a factor of 3 to ~4.5 million km^2, by summer (average 2011–2019; National Snow and Ice Data Center, 2020). Moreover, in winter there is about 1.65 million km^2 of landfast sea ice, that reduces to near zero in summer (Li et al., 2020). The presence of landfast ice can significantly affect local hydrodynamics as it prevents interaction between the atmosphere and underlying ocean (Mahoney et al., 2014).

While an ice cover shields the ocean from atmospheric forcing, it also exerts additional frictional stress on the surface. Early studies demonstrate that drag between water and ice results in tidal dampening, especially in coastal zones where ice is relatively immobile (Godin, 1986; Kowalik, 1981). Kowalik (1981) showed that the presence of sea ice can lead to tidal amplitude decay and phase delay. More recent studies have looked specifically into the modulation of tides in the Arctic region in response to a seasonally varying ice cover and suggest the effect to be substantial; in some regions changing the amplitude by up to 0.15 m (Kagan & Sofina, 2010; St-Laurent et al., 2008). This implies that it is insufficient to regard tides as constant throughout the year and ignore the influence of sea ice, which is done in most operational tide models. For accurate prediction of Arctic tidal water levels, quantification of seasonal modulation is necessary. In addition, studies have shown that Arctic tides directly affect North Atlantic tides (Arbic et al., 2004, 2007),
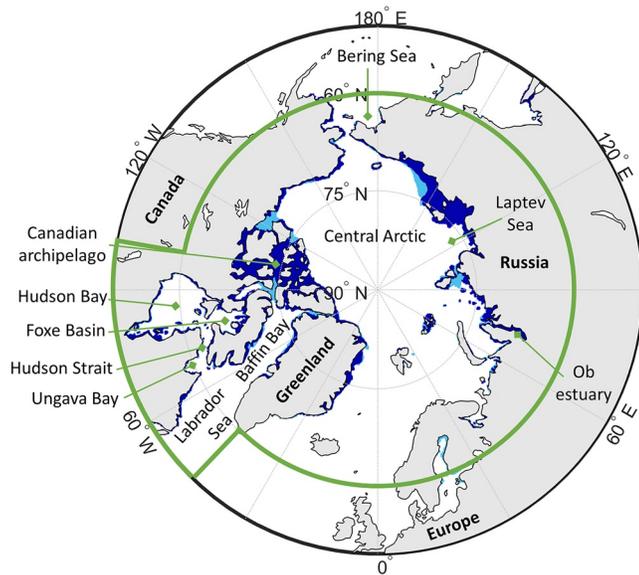
Figure 1. Arctic landfast ice extent for March 11, 2013 (light and dark blue) and March 9, 2017 (dark blue), obtained from updated dataset of U.S. National Ice Center (2009). Note that the ice cover of 2017 completely overlaps that of 2013. The green outline indicates the domain of our study.

implying that the influence of Arctic sea ice on tides extends beyond the Arctic.

Müller et al. (2014) modeled seasonal variations in the M_2 tide on a global scale, forced by annual differences in stratification and sea ice cover. While they incorporated altimeter-derived sea level data in their study, only in situ data were considered for the high latitudes. Other numerical studies that focused on the Arctic were often restricted to a certain region, for example, the Central Arctic and Russian shelf (Kagan & Sofina, 2010) and the Hudson Bay system (Kleptsova & Pietrzak, 2018; St-Laurent et al., 2008). In addition, tide monitoring in the area is limited. Hence, models that link seasonal variations in sea ice to modification of Arctic tides can only be validated locally and the large-scale signals remain uncertain.

For the first time, in this study, the seasonal modulation of the largest tidal constituent M_2 is quantified for the entire Arctic. To achieve this, we supplement data from the sparse set of Arctic tide gauges with data from Synthetic Aperture Radar (SAR) altimeters. The latter provide water level information up to 88°N, including predominantly ice-covered areas. Then, we model the effect of landfast ice on the Arctic M_2 tide for summer and winter landfast ice configurations, providing insight in the extent to which landfast ice is responsible for the Arctic tidal modification. Finally, we use the model to simulate the global effect of variations in Arctic landfast ice cover, which we then relate to observed seasonal modulation at tide gauges across the globe.

2. Methodology

2.1. Evaluating Seasonal Modulation From Altimetry

There are very few tide gauges in the Arctic and only some of them have data publicly available. Furthermore, the usage of altimetry to derive tidal measurements is limited at high latitudes, because this area is not covered by the radar altimeter satellites that are typically used for this purpose (e.g., TOPEX/Poseidon and Jason Müller et al., 2014). Added to this, the low along-track resolution of conventional low-resolution mode altimeters does not allow for distinguishing between measurements from the sea ice pack and alternating narrow sections of open water. Therefore, this study made use of data from two high-inclination satellite altimeter missions: CryoSat-2 (CS2; Wingham et al., 2006) and Sentinel-3 (S3; Donlon et al., 2012). CS2, launched in April 2010, has a ground coverage up to 88°N/S, and S3, launched in February 2016, reaches latitudes up to 81 0.5°N/S. The typical cross-track spacings of both satellites are ~50 km at 60°N and ~ 18 km at 80°N. Both missions are equipped with a SAR altimeter that is active over Arctic waters, resulting in a high along-track resolution (~300 m). The latter is a significant advantage, as it enables obtaining water levels from leads; i.e., open-water fractures in the sea ice pack (e.g., Schulz & Naeije, 2018; Wernecke & Kaleschke, 2015). This allows for more complete and year-round information on the sea surface height, even in areas that are usually covered by sea ice. Year-round data are necessary for proper derivation of seasonal variations in tides. Data were collected for the region north of 60°N, extended by the Hudson Bay area; 50°N –60°N, 100 -45°W (see Figure 1). Acquisition times of the used data range from June 2010 to August 2019 (CS2) and from December 2016 to December 2019 (S3).

SAR returns from sea ice, leads, and open water were classified according to a multi-criteria classification scheme inspired by Poisson et al. (2018); Schulz and Naeije (2018) and Wernecke and Kaleschke (2015). The used criteria are specified in Table 1. After classification, we retracked the signals of water classes by fitting the SAMOSA model (Dinardo et al., 2018; Ray et al., 2015). In contrast to conventional open water retracking, we distinguished two cases. In case of open ocean returns, the epoch t_0, significant wave height (SWH) and signal amplitude P_u were estimated, while ν (inverse of the mean square slope of the sea surface) was set to 0 and not estimated (in line with Dinardo et al., 2018). However, for leads the sea surface is relatively

Table 1
Multi-Criteria Classification Scheme for SAR Return Signals

	Open ocean	Leads	Sea ice
Sigma0	0–10 dB	>25 dB	–
PP	<0.065	<0.25	<0.15
PPloc	<0.3	–	–
Ptail	20–45	<0.5	–
RatioIP	–	<0.65	–
No. of peaks	1	1	>1
	or:		**or**:
Kurtosis	5–15	–	>12

Note. Where: Sigma0 is a measure for the magnitude of the return signal, PP (pulse peakiness) and PPloc describe the normalized power of the peak with respect to respectively the total reflected power (after laxon, 1994) and the 10 bins surrounding the peak, Ptail describes the normalized power in the tail of the return signal and ratioIP the ratio between the power in the leading edge and the tail. Kurtosis is only considered if a signal fulfills all criteria for a class except the number of peaks.

smooth and we fixed SWH to 0, while ν was estimated and allowed to be infinitely large (following Jain et al., 2014).

Compared to satellites that are conventionally used for measuring tides (e.g., TOPEX/Poseidon and Jason), CS2 and S3 have a long revisit time: CS2 has a 369 days repeat cycle (with a 30-days sub-cycle) and S3 has a repeat cycle of 27 days. This results in alias periods of 112.1 days (CS2) and 157.5 days (S3) for M_2 and does not allow for along-track tidal analysis. To overcome the low temporal resolution, we stacked the data using a $3° \times 1°$ grid (~100 km), following Cancet et al. (2018). Subsequently, the data for each grid cell were combined into one timeseries assigned to the data centroid of the cell. Data were omitted when less than 1,000 observations were available in a cell or when more than 30 sequential days in the year do not have data in the cell.

From the full timeseries (2010–2019) of each grid cell, tidal amplitudes and phases were estimated using UTide (Codiga, 2020). UTide executes harmonic analysis for a given set of frequencies similar as in T_TIDE (Pawlowicz, 2002), yet it is able to deal with irregular temporal sampling. The latter is a requirement for processing altimeter-derived water levels. Tidal constants were estimated for major tides; K_1, O_1, Q_1, P_1, N_2, M_2, S_2 and K_2, and the two satellite constituents of M_2; H_1 and H_2. The latter describe the annual modulation of the M_2 tide (Zijl et al., 2016). Thereafter, a yearly signal was reconstructed based on only M_2, H_1 and H_2. At this stage, the 18.61 years nodal modulations were omitted to eliminate interference with the seasonal amplitude modulation. From the reconstructed signal, yearly and monthly average amplitudes/phases and the magnitude of annual variations were computed. Monthly average values were obtained for March and September for comparisons with model simulations.

2.2. Evaluating Seasonal Modulation From Model

2.2.1. Model Description

To obtain the seasonal modulation of M_2 under the influence of a seasonally varying landfast ice extent, we used the operational Global Tides and Surge Model (GTSM) (Verlaan et al., 2015). This depth-averaged barotropic model is forced by a full tidal potential and developed in Delft3D Flexible Mesh on an unstructured grid with 25 km (open ocean) to 2.5 km (coast) resolution. To prevent a singularity at the North pole (caused by the regular grid) and an unnecessary refinement near the poles, an unstructured grid was used with the North Pole being a node in itself and the grid spanning out from there (see Verlaan et al., 2015). The model uses the GEBCO2019 gridded bathymetry data set, which involves IBCAOv3 for the Arctic bathymetry (GEBCO Compilation Group, 2019). This bathymetry is continually developing, hence, to account for any uncertainties in the bathymetry an estimation procedure is employed (Wang et al., 2021) which uses a data assimilation framework with observations for the deep ocean tides obtained from FES2014 global tide model. The global tide model performance of GTSM was evaluated in Wang et al. (2021), and an additional analysis with specific focus on the Arctic is available in Text S1. Atmospheric forcing was not considered during the simulations.

The effect of sea ice was not included in the version of GTSM described by Wang et al. (2021). However, a sea ice cover may have a strong influence on the tidal dissipation rate (Kagan et al., 2007). This dissipation results from the friction between the sea ice and the underlying ocean and thus depends on the mobility of the sea ice. We have incorporated this dissipation in the model as an additional frictional shear stress, parameterized with a quadratic drag law in line with Kagan and Sofina (2010), Müller et al. (2014) and St-Laurent et al. (2008). The formulation used for ice-ocean shear stress (τ_i) is:

$$\boldsymbol{\tau_i} = \rho_w C_{d_i} \boldsymbol{u_i} - \boldsymbol{u}(\boldsymbol{u_i} - \boldsymbol{u}), \tag{1}$$

where $\boldsymbol{u}$ is the tidal velocity vector, $\boldsymbol{u_i}$ the ice drift velocity vector, ρ_w is the density of sea water (1,024 kg/m^3). C_{d_i} is the ice-water drag coefficient whose magnitude varies from 1.32 to 26.8 $\times$ 10^{-3} (Langleben, 1982; Madsen & Bruno, 1987; Pease et al., 1983; St-Laurent et al., 2008). In our study, it was assumed to be 5.5 $\times$ 10^{-3} in accordance with McPhee (1980) and Hibler (1979).

Since GTSM is not coupled to an ice model, it is not possible to obtain ice velocities at every time step. This limited our capability to compute the shear stress (Equation 1) for non-zero ice drift velocity. However, the state of the sea ice has two bounds: Ice-free surface and fixed ice (landfast ice) (Kagan & Sofina, 2010). In the latter case, the drift velocity is equal to zero ($\boldsymbol{u_i} = 0$) which makes it possible to evaluate Equation 1.

The ice-water frictional stress was introduced only for the regions of landfast ice cover in the domain. The remaining domain was considered to have no frictional dissipation due to this stress. The regions of landfast ice cover were modeled by means of polygons outlining their extent (Cancet et al., 2018). These polygons were created using an updated version of gridded U.S. National Ice Center sea ice charts, at 10 km resolution (U.S. National Ice Center, 2009).

2.2.2. Quantifying Seasonal Modulation

We estimated the effect of landfast ice on seasonal modulation of tides by comparing M$_2$ amplitudes and phases from two model simulations with seasonal limiting cases of fast ice cover. We followed the approach of St-Laurent et al. (2008) and used the landfast ice covers of March and September, corresponding to the annual maximum and minimum landfast ice cover respectively (U.S. National Ice Center, 2009). Here, we assumed the landfast ice induced tidal modification to be strongest in case of maximum landfast ice cover, and the change in tidal constants between the two limiting cases to be monotonic. This assumption was supported by a series of simulations based on monthly landfast ice covers of 2013 (see Text S2).

To assess the impact of inter-annual variations in landfast ice cover, simulations were done for 2013 and 2017. These years had, respectively, the maximum and minimum fast ice cover within the time span of the considered SAR data (2010–2019) (Li et al., 2020). In both years there was only a negligible amount of landfast ice cover in September. Therefore, we considered no fast ice in the September simulations, leading to the first limiting case of ice-free surface. The March landfast ice-extents are shown in Figure 1.

Simulations were done for 29.5 days, preceded by a 7-days spin up time. This period of 29.5 days corresponds to two spring-neap cycles and is sufficiently long for disentangling M$_2$ from the other tidal constituents involved in the analysis. Note that this period does not allow accurate separation of S$_2$ and K$_2$, and K$_1$ and P$_1$, as this requires a timespan of 182.6 days (Foreman & Henry, 1989). Although this may have a minor effect on the estimation of M$_2$, it will not impact our analysis since we compare amplitudes/phases between March and September. These months are half a year apart and therefore in phase with the semi-annual cycle resulting from the superposition of these constituent pairs. Hourly water levels were saved for the locations of the stacked SAR data (see Section 2.1). Subsequently, tidal constants were estimated using UTide (Codiga, 2020) for the same set of major constituents as described in Section 2.1, but excluding H$_1$ and H$_2$. Nodal corrections were applied to eliminate amplitude differences caused by the 18.6 years nodal cycle. This allows direct comparison between estimated M$_2$ phases and amplitudes from the different simulations.

To compare model- and altimeter-derived seasonal modulation, root mean square errors (RMSE) and normalized root mean square errors (nRMSEs) were calculated as follows, where y represents the considered variable either derived from observations (y_{obs}) or from the model (y_{model}) and n the number of observations:

$$RMSE = \sqrt{\frac{1}{n}\Sigma_{i=1}^{n}\left(y_{obs} - y_{model}\right)^2}, \tag{2}$$

$$nRMSE = \frac{\sqrt{\frac{1}{n}\Sigma_{i=1}^{n}\left(y_{obs} - y_{model}\right)^2}}{\sqrt{\frac{1}{n}\Sigma_{i=1}^{n}\left(y_{obs}\right)^2}}, \tag{3}$$

2.2.3. Global Effect

Finally, to study the impact of seasonal variations in Arctic landfast ice on global tides, we additionally stored modeled water levels on a $1° × 1°$ global grid (in addition to the locations of the SAR data). This was done for all simulations mentioned in the previous section; that is, March and September, 2013 and 2017. M_2 amplitudes were estimated as described in Section 2.2.2.

Estimated amplitudes were then compared to March and September M_2 amplitudes derived from a global set of tide gauge records for corresponding years, obtained from the University of Hawaii Sea Level Center (Caldwell et al., 2015). Monthly amplitudes were estimated from the tide gauge records using UTide and following the same approach as was adopted for altimeter data (see 2.1). Tide gauge stations with large interannual variation in March-September amplitude differences (standard deviation (std) > average amplitude difference, based on 2000–2019) and those where the value of the year in question was an outlier (value > average amplitude difference ± 2∗std), were excluded from the analysis.

3. Results

3.1. Altimeter-Derived Seasonal Modulation in the Arctic

Altimeter-derived yearly average M_2 amplitudes range from near zero in the Central Arctic to over 1.5 m in Hudson Strait (Figure 2a). All tides in the study domain travel anticlockwise (Figure 2b, see Figure 4a for location of amphidromic points).

The total annual seasonal modulation of M_2 amplitudes ranges up to ∼0.25 m (Figure 2c) with the largest ranges in Hudson Bay, Hudson Strait, Foxe Basin and along the Russian coastline (see Figure 1 for locations). In the Central Arctic, large annual phase modulations (up to 180°) were observed, which may be an artifact of very low amplitudes (<0.05 m, see Figure 2a) combined with low data availability during winter (see Figure S3), disabling proper estimation of phase variations. These data will therefore not be considered in further analysis (hatched region in Figure 2d and 5b). The largest variations in M_2 phase occur near the coasts of Russia and Canada (up to 45°).

The relative magnitude of seasonal modulation, that is, the total annual modulation divided by the yearly average M_2 amplitude (Figure 3b), is largest in the Canadian archipelago and Bering Sea where amplitudes are relatively low, and smallest in the European seas. The timing of seasonal modulation varies widely across the different regions. Most of the Canadian archipelago and Russian shelf experience highest M_2 amplitudes in summer months, while in Baffin Bay and the European seas, maximum M_2 amplitudes are predominantly observed in winter/spring (Figure 3c). In Hudson Bay, there is a near equal division between regions that experience maximum M_2 amplitudes in winter and in summer. In the Central Arctic and Bering Sea, largest amplitudes are observed in early summer.

In addition, March and September M_2 amplitudes are compared directly (Figures 3d and 5a). Amplitudes are often lower in March than September in the Canadian archipelago and on the Russian shelf (except for Laptev Sea, see Figure 1), while in Hudson Bay and the Bering Sea there is larger variability. In the Baffin Bay region, amplitude differences are predominantly positive, except for the Greenland fjords that are covered by landfast ice during March (Figure 1). Comparing Figure 5a with Figure 2c shows that in most of the Arctic the absolute March-September amplitude difference and the maximum seasonal modulation correspond closely. However, in Hudson Strait, Foxe Basin, southern Hudson Bay and the Ob estuary (Russia, see Figure 1), there are larger differences between the two measures (Figures 2c and 5a). This is in line with Figure 3c, where we showed that in several regions maximum amplitudes are observed in early summer rather than either March or September.

In most of the Central Arctic, the Canadian archipelago and Baffin Bay phase differences are positive, indicating later arrival of the tide (phase delay) in March (Figures 3e and 5b). This is in contrast to Hudson Bay, where the phase is predominantly advanced (negative difference). Moreover, there are amphidromic points that shift up to 100 km between March and September: In Hudson Bay to the northeast, and on the Russian shelf to the west (Figure 4a).
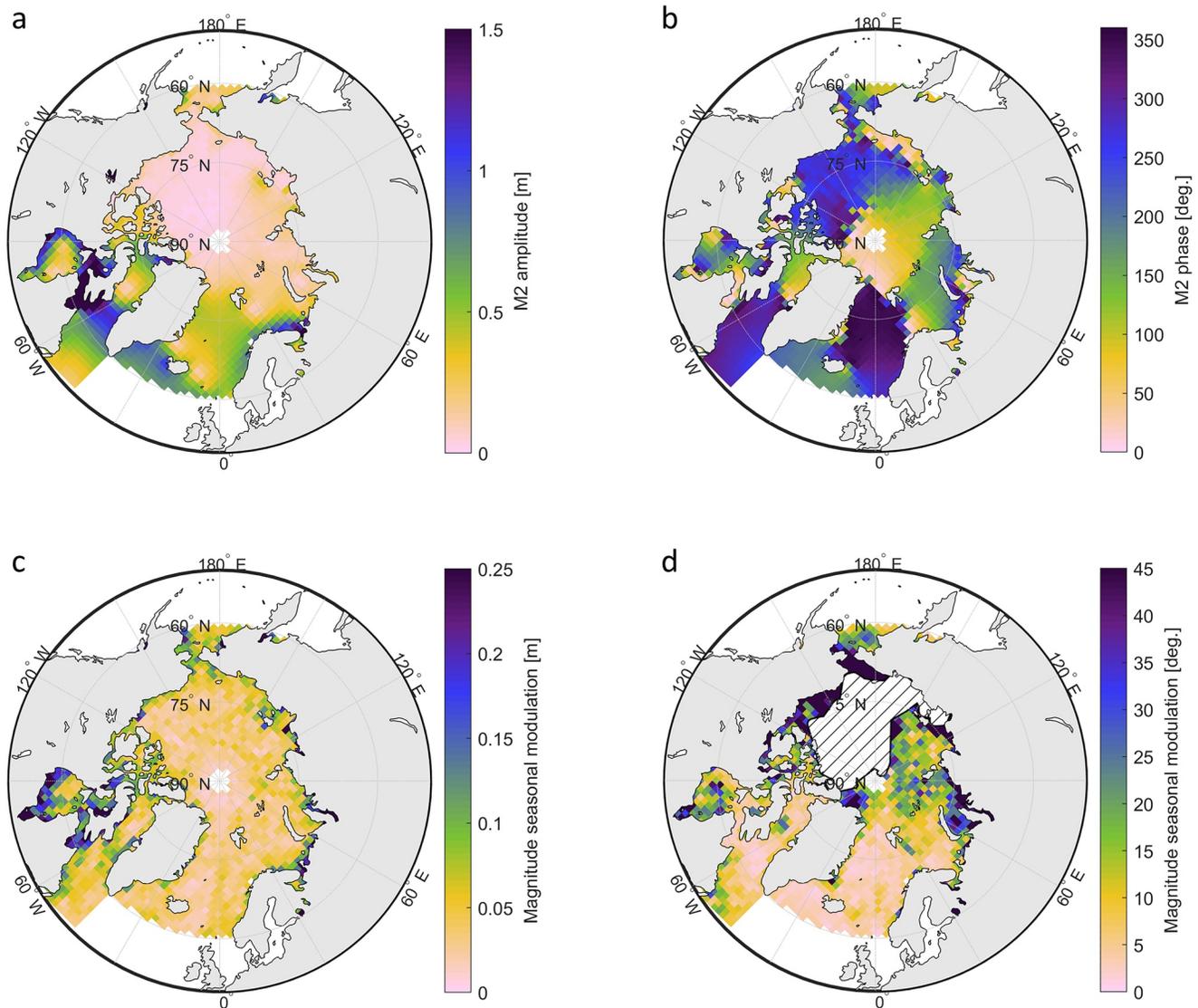
Figure 2. Altimeter-derived yearly average M$_2$ amplitude (a) and phase (b) and magnitude total annual modulation of M$_2$ amplitude (c) and phase (d). Hatched region indicates unreliable phase data that are not further considered. Data have been interpolated to a stereographic grid for plotting.

3.2. Modeled Seasonal Modulation in the Arctic

Modeled seasonal modulation for 2013 (Figures 5c and 5d) compared with altimeter-derived modulation (Figure 6) shows that, although there is larger variability in altimeter-derived modulation, the predominant observed signal corresponds to the model-derived modulation in several regions. Altimeter-derived and model-derived differences in M$_2$ amplitude between March and September are negative in the Canadian archipelago and on the Russian shelf, positive in Baffin Bay and close to zero in the Arctic Ocean and European seas (Figures 5c and 6a). However, in Hudson Bay—and to a smaller extent, the Canadian archipelago and Bering Sea—positive differences are not captured well by the model. This results in large deviation with respect to altimeter-derived values and a large RMSE (0.21 m) and nRMSE (1.29; Figure 6c). While nRMSE values are large for all of the regions, this can in part be attributed to the larger variability in altimeter-derived modulation (Figure 6a). In addition, model-derived differences in amplitude are in most cases lower than those derived from observations, by up to 0.1 m (Figures 5a, 5c, and 6).

Model-derived phase differences correspond relatively well for Hudson Bay (predominantly negative) and the Canadian archipelago (predominantly positive) (Figures 5b, 5d, and 6d). In Baffin Bay and the European
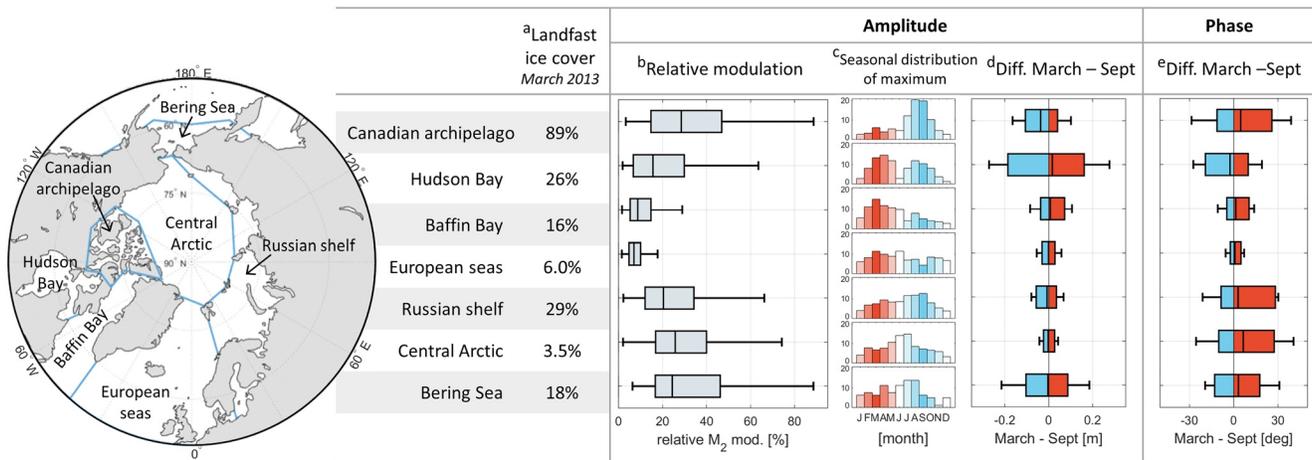
Figure 3. Overview of altimeter-derived seasonal modulation of M_2 for different subregions (indicated on the left). Landfast ice cover (a) is calculated as the number of data points covered by landfast ice divided by the total number of data points in each region. Relative seasonal modulation (b) is calculated by dividing the total annual modulation (Figure 6c) by the M_2 amplitude (Figure 6a). The seasonal distribution of maximum (c) shows for each month the percentage of data points within the subregion that experience maximum M_2 amplitudes during that month. Here, Arctic summer months are displayed in blue and winter months in red, as they respectively relate to a negative (blue) or positive (red) March-September difference in amplitude (d). March-September differences (d), (e) show the median, 10th and 90th percentiles of all values in the region.

seas, both model and observations produce low phase differences, resulting in a small RMSE (≤15°). For the Russian shelf, Central Arctic and Bering Sea, modeled phase differences have a significantly smaller spread compared to altimeter-derived differences (up to 20°). In addition, the extent of the observed shifts in amphidromic points is not well captured by the model. In fact, in Hudson Bay the model-derived shift is in the opposite direction compared to what was observed (Figure 4b).

The model-derived amplitude and phase differences caused by the smaller landfast ice cover of 2017 (not shown here) display a similar pattern as in the case of 2013. In most of the domain, there is little difference between the March amplitudes of both years. However, the differences are significant in Hudson Bay and nearby regions; up to 0.05 m (~20%) (Figure 5e). In general, this results in reduced differences between March and September amplitudes in 2017. Negative differences in amplitude are reduced by up to 0.05 m in Hudson Bay and positive differences in Hudson Bay (east) and Baffin Bay are reduced by about 0.02 m. Seasonal modulation is larger in 2017 (up to 0.02 m) than in 2013 in the east of the Canadian Archipelago and in Labrador Sea. The east of the Canadian Archipelago is not covered by landfast ice in 2017, while it was in 2013, and has a lower M_2 amplitude in March 2017 than in 2013. This results in a larger amplitude difference in March with respect to September. In the Labrador Sea, the March amplitude of 2017 is more positive than that of 2013. In March 2017, Hudson Bay experiences less phase advance than in March 2013. In the Central Arctic, the Canadian archipelago, Baffin Bay and on the Russian shelf, phase delay is reduced as well. Nevertheless, the effect of interannual variations in landfast ice cover on model-derived seasonal modulation is smaller than the differences with respect to altimeter-derived modulation.

3.3. Global Effect of Arctic Landfast Ice

The modeled effect of seasonal change in landfast ice extent on the seasonal modulation of tides is not restricted to the Arctic (Figure 7). Different March and September M_2 amplitudes are derived across the globe, although the values are significantly smaller south of ~50°N (up to 0.05 m) than in the Arctic. Overall, the magnitude of amplitude differences is related to the yearly average amplitude (see Figure 8a). However, no seasonal modulation was modeled for the Bay of Bengal (east of India, amplitudes up to 1 m) and some parts of open ocean where yearly average amplitudes are relatively large; for example, the Indian and Pacific Oceans. In contrast, amplitude differences are observed in some regions with relatively small amplitudes. In these cases the amplitude differences are predominantly negative; for example, west of northern Africa, southwest of Australia, west of Chile and east of Japan (Figure 7). There are small differences between the model-derived seasonal modulation for 2013 and 2017. In several regions with a positive March-September
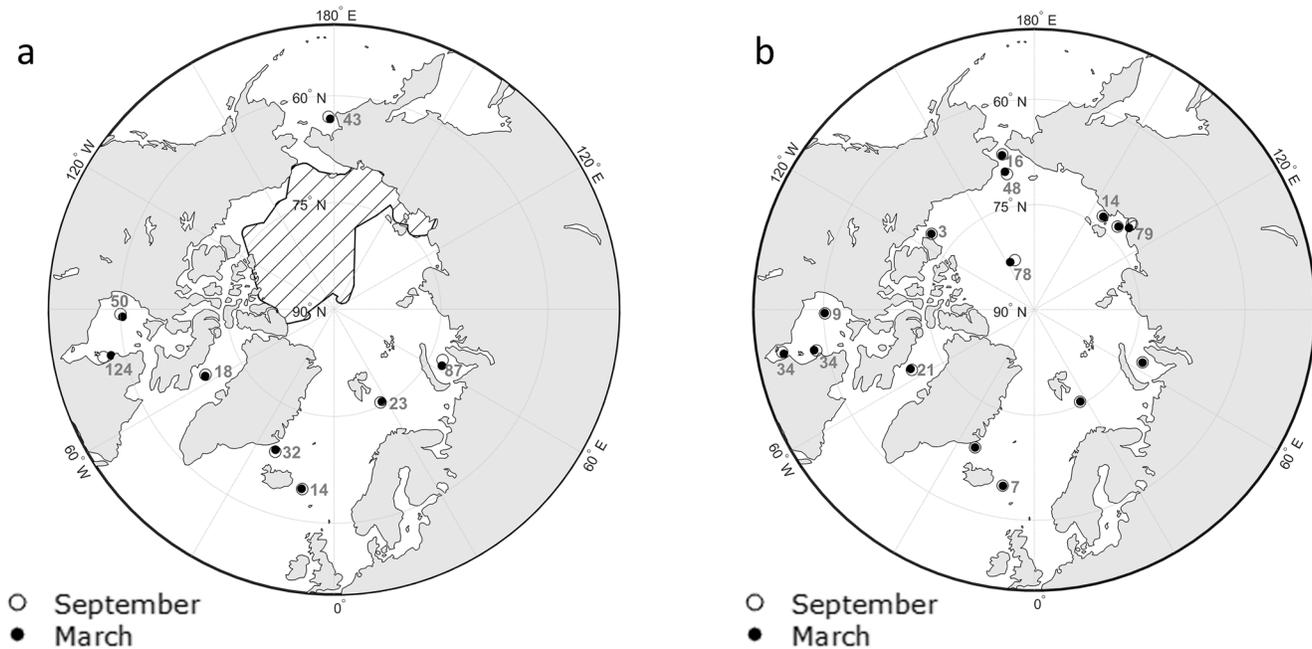
Figure 4. Location of amphidromic points in September and March derived from altimetry (a) and GTSM (b). Distance between each pair is indicated in gray (km). Hatched region indicates unreliable phase data that is not considered in further analysis.

amplitude difference in 2013 (e.g., Gulf of Alaska, Gulf of Biscay and the area north of Brazil), these differences are up to 0.02 m larger in 2017. In contrast, the positive amplitude difference near Madagascar and west of India is reduced in 2017 by a similar extent. In other regions where there was a negative March-September amplitude difference in 2013 (e.g., along the coasts of Chile and Antarctica), these differences are reduced by ∼0.02 m in 2017.

The degree of correspondence between model-derived seasonal modulation and modulation derived from tide gauge records, varies regionally (Figure 7). Around Europe, New Zealand, the Arabian Sea, northern gulf of Alaska (2013), the Antarctic Peninsula (2013) and along the coast of Chile, the model-derived and observed differences in amplitude are of similar sign and magnitude. However, inconsistency is observed in other regions. For instance, the local variability as observed in the seasonal modulation derived from tide gauges in the waters around east Asia and along the east coast of North-America, is not present in the modeled signal. Regional examination (Figure 8) shows best agreement between modeled and tide gauge-derived seasonal modulation in Europe, N-America east, the Indian Ocean and Antarctica (2013). Overall, the agreement is slightly better in 2013 than in 2017. Nonetheless, this direct comparison highlights areas where the model largely deviates from observations and the RMSEs and nRMSEs are large (Figures 8e and 8i). Most noticeable examples are N-America west, the Gulf of Mexico, South America and East Asia. Model-derived differences between 2013 and 2017 correspond to observed differences for the tide gauges along the coast of Chile, but not for all tide gauges in the Gulf of Alaska. For the other regions we cannot compare tide gauge data of 2013 and 2017, since there was no data for either one of the 2 years.

4. Discussion

We studied the seasonal modulation of the Arctic M_2 tide based on SAR altimetry-derived water levels, then linked these to seasonal variations in ice cover using the GTSM. This resulted in the first observation-based quantification of the seasonal modulation of the M_2 tide for the entire Arctic. Here, we combined data from two high-inclination satellite missions (CryoSat-2 and Sentinel-3) to ensure full (year) coverage of the Arctic waters. We stacked data from multiple tracks on a grid basis (following Cancet et al., 2018) to account for the low temporal resolution and irregular availability of the data. This approach minimized issues related
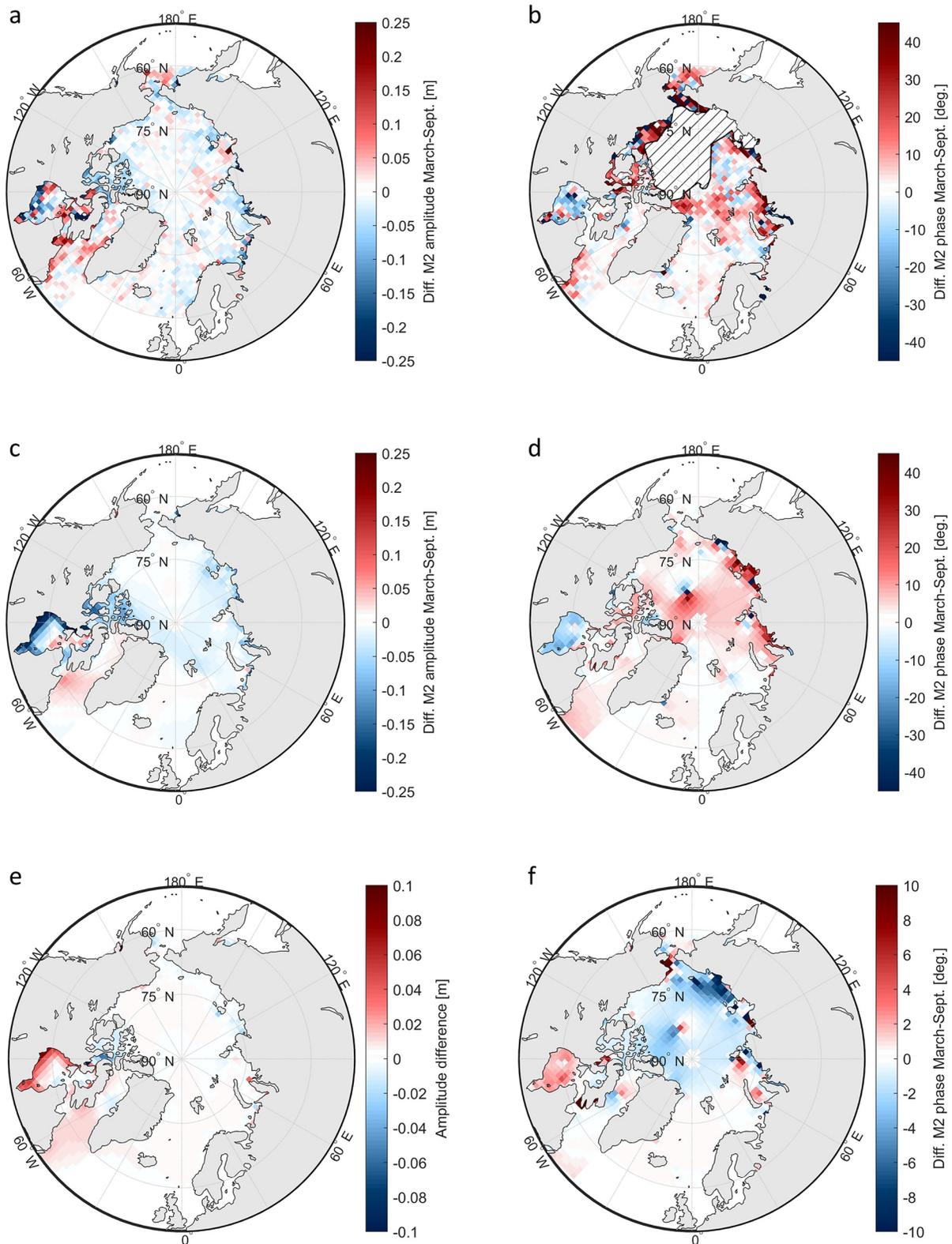
Figure 5. Altimeter-derived differences between March and September M$_2$ amplitudes (a) and phases (b) and model-derived differences in amplitude (c) and phase (d) for 2013. Bottom figures display the model-derived difference in amplitude (e) and phase (f) between March 2017 and March 2013 (2017–2013; different color scale). Hatched region indicates unreliable phase data that is not considered in further analysis. Data have been interpolated to a stereographic grid for plotting.
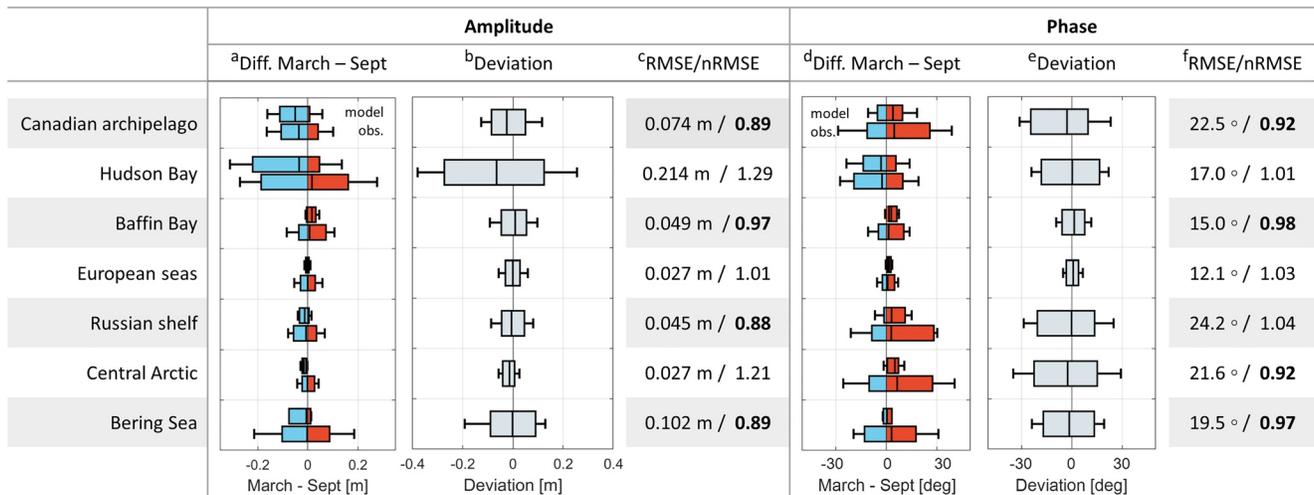
Figure 6. Overview of model performance with respect to altimeter-derived seasonal modulation for the subregions as in Figure 3. March-September differences (a), (d) show first the model-derived differences for each region (2013) followed by altimeter-derived differences as in Figure 3. Deviation (b), (e) shows the median, 10th and 90th percentiles of modeled March-September differences minus altimeter-derived values. RMSE and nRMSE (c), (f) are calculated according to Equations 2 and 3 respectively.

to inseparable constituent pairs and aliasing, which would arise in conventional along-track tidal analysis (Cancet et al., 2018; Savcenko & Bosch, 2007).

Altimeter-derived seasonal modulation was compared to earlier studies that computed seasonal variations in M_2 amplitudes based on water level records from tide gauges or temporary pressure sensors. Comparable seasonal changes in amplitude and phase (magnitude and timing) were observed along the Russian coast (Kulikov et al., 2018); in most of Hudson Bay (Kleptsova & Pietrzak, 2018; St-Laurent et al., 2008) and in the Labrador Sea and Canadian archipelago (Kleptsova & Pietrzak, 2018). In northern Hudson Bay, altimeter-derived differences between March and September amplitudes were more positive than those derived from in situ data (St-Laurent et al., 2008). This difference may be caused by interannual variability; where our study is based on altimeter data from 2010 to 2019, St-Laurent et al. (2008) studied sea level data from August 2003 to August 2006.

There have been several attempts to quantify the seasonal modulation of the Arctic M_2 tide using tide models, although most of them were focused on the Hudson Bay area. These studies suggested various magnitudes of seasonal modulation. For instance, Müller et al. (2014) used a global ocean circulation and tide model (STORMTIDE) with an embedded sea-ice model and studied the effect of both ice cover variations and changes in stratification. They suggested a seasonal amplitude change up to 0.15 m (yearly max-min) in Hudson Bay. In contrast, Kleptsova and Pietrzak (2018) indicated that variations in the (total) sea ice cover alone cause a seasonal modulation that is up to tenfold larger. This is high compared to our altimetry-derived seasonal modulation in the area (0–0.25 m; Figure 6c). Kleptsova and Pietrzak (2018) attributed the deviation between their model output and in situ observations to the use of constant boundary conditions at the eastern entrance of Hudson Strait. St-Laurent et al. (2008) specifically compared M_2 March and September amplitudes (consistent with our approach), obtained from a 3D ocean model coupled to a sea-ice and snow model. According to their simulations, amplitudes differed up to 0.15 m. This is similar to the values we obtained (Figure 5a). However, they computed a negative amplitude difference in the western part of Hudson Bay and in Ungava Bay which contradicts the altimeter-derived values. Their outcome does largely correspond to our model-derived differences in amplitude (Figure 5c), even though our approach was more simplified. In addition, Kagan and Sofina (2010) modeled seasonal modulation of the M_2 tide on the Russian shelf and Central Arctic using a three-dimensional model with an ice drift module included. Their results are comparable to our altimeter- and model-derived values for amplitude and our model-derived modulation of the phase, in terms of magnitude and sign.
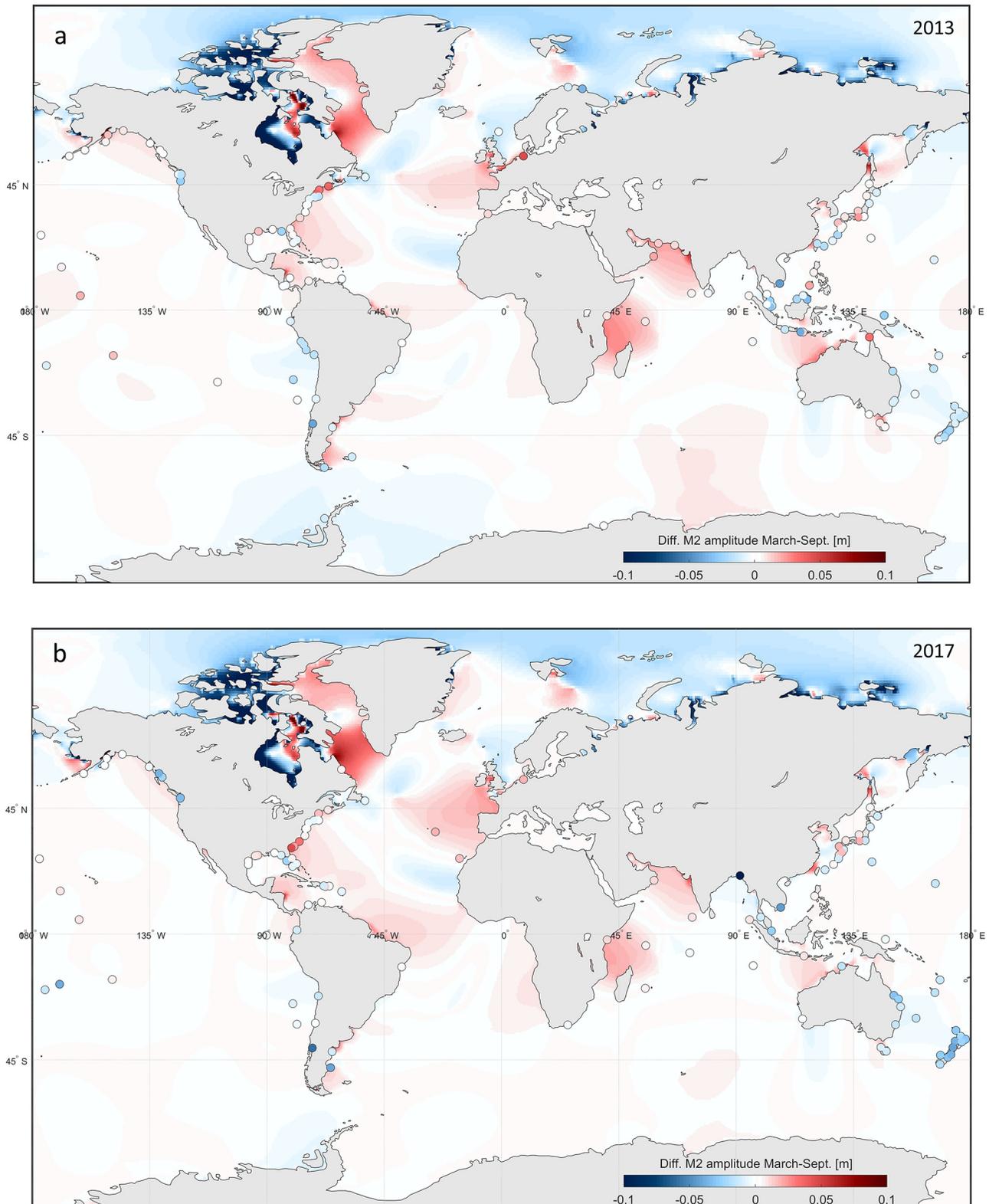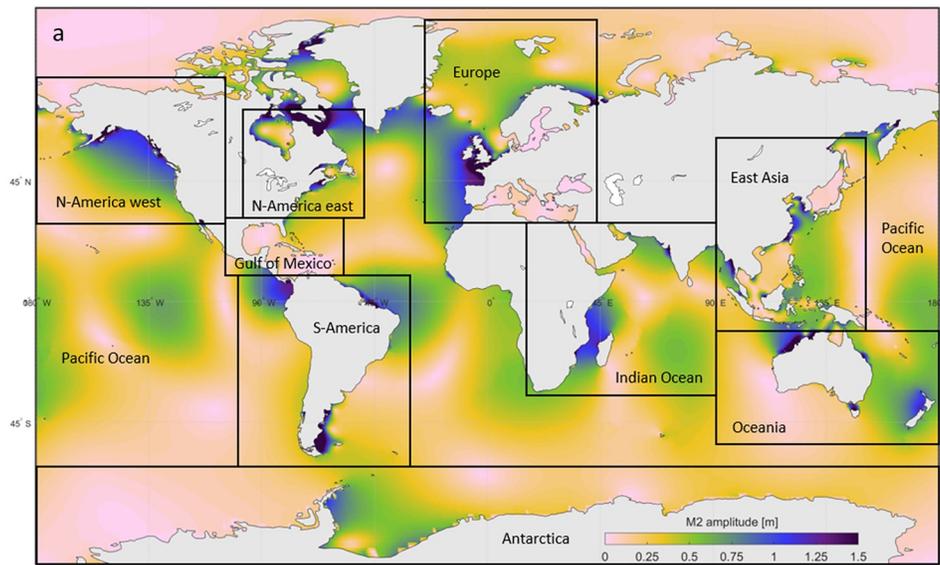
Figure 7. Difference between March and September M$_2$ amplitude as derived from tide gauge records (circles) and as modeled under the influence of Arctic landfast ice cover (background map) for 2013 (a) and 2017 (b).

Figure 8. Overview of model performance with respect to tide gauge-derived seasonal modulation globally for 2013 and 2017 for regions defined in (a). The background of (a) shows the yearly average modeled M_2 amplitude. No. TG (b), (f) depicts the number of tide gauges included in each comparison (outliers excluded). March-September differences (c), (g) show first the model-derived differences for each region followed by tide gauge-derived differences. Deviation (d), (h) shows the median, 10th and 90th percentiles of modeled March-September differences minus tide gauge-derived values. RMSE and nRMSE (e), (i) are calculated according to Equations 2 and 3 respectively.

In agreement with previous observations and model simulations, the results presented in this study shows that a landfast ice cover in one location typically leads to local amplitude decrease (Prinsenberg & Freeman, 1986; Sverdrup, 1927). Moreover, observed and modeled phase advance in Hudson Bay and phase delay in other regions are in line with earlier theoretical considerations (Prinsenberg & Freeman, 1986). According to the latter, increased friction results in reduced phase velocities and thus a larger phase lag. However, in Hudson Bay, the interaction between the incoming and reflected wave causes a change in phase/amplitude patterns, and the net phase is advanced (Prinsenberg & Freeman, 1986). Amplitude decrease is clearly visible in the Canadian archipelago and on the Russian shelf where the landfast ice cover is large. However, in Hudson Bay, Ungava Bay, Labrador Sea and part of Bering Sea, the opposite effect is observed. Here, areas that are not covered by landfast ice show an increase in amplitude during March, suggesting a complex relation between ice in one location and a far-field effect on tides in another. This was previously shown by Kagan and Romanenkov (2007), whose modeling study indicated that the ice-covered White Sea

caused an amplitude increase in the ice-free Barents Sea. In Hudson Bay, the observed increase in amplitude at the western coast and, to a smaller extent in the southern part can be related to the observed shift of amphidromic points away from these areas. The latter was not captured by the model and contradicts earlier studies (Kleptsova & Pietrzak, 2018; Prinsenberg & Freeman, 1986). This suggests that the shift might be caused by other seasonal processes besides variations in landfast ice cover. Moreover, the observed tidal amplification in Labrador Sea is in line with Arbic et al. (2004), who linked this to ice cover presence in Ungava Bay/Hudson Strait. In addition, Arbic and Garrett (2010) showed that increased friction in Hudson Strait results in increased amplitudes along the North Atlantic coast. This is consistent with our simulated seasonal modulation and the modulation derived from tide gauges (Figure 7). Figure 7 even suggests such effects to be noticeable on a global scale. However, note that we observed significant differences between model- and tide gauge-derived seasonal modulation (Figure 8) in specific regions and that the seasonal modulation derived from tide gauge records is likely the result of multiple (regional) processes. Regardless, it has been shown that the sensitivity of the model to landfast ice reaches well beyond the Arctic. We expect that similar (yet out of phase) responses will be present due to variations in extent of landfast ice around Antarctica.

Although many of the observed differences in amplitude and phase are to a certain extent captured by our model, there is no complete agreement. In particular, the positive differences in amplitude (larger amplitudes in March than in September in Hudson Bay, Hudson Strait, Bering Sea, Laptev Sea) are not captured by the model. However, the model only considers the effect of seasonal variations in landfast ice on the tide and other effects were deliberately ignored. For example, including drifting sea ice (with strong internal stresses) in the model, may lead to enhanced seasonal modulation. However, this is not likely to explain the positive amplitude differences in Hudson Strait as this was also not obtained by St-Laurent et al. (2008), who did consider drifting ice. In addition to this, for such drifting sea ice the imposition of wind forcing could result in a different frictional stress at the ice-ocean interface as opposed to the case of drifting ice without winds (Hibler et al., 2006). This might further affect tidal amplitudes and phases. Wind variations have also been connected to seasonal modulation of tides on the northwest European shelf (Zijl et al., 2016), but were not included in our model setup. Finally, as GTSM is a two-dimensional model with assumed uniform density, the effect of spatial density differences and stratification was not considered. Spatial differences in density (i.e., baroclinic pressure gradients) influence the movement of water and therefore the mean water level (Zijl et al., 2013). Especially in the Hudson Bay system, adjustments of the mean sea level affect local tides (Pickering et al., 2017). Stratification impacts the stability of a water column and thus the amount of energy lost into turbulent processes. On the one hand, a stratified water column is more stable, which could result in more pronounced tidal transport and surface tides, compared to well-mixed conditions (Müller, 2012; Müller et al., 2014). On the other hand, stratified conditions have been associated with the generation of internal tides, which can cause local dissipation of barotropic energy (Müller, 2012; Müller et al., 2012). Considering these (local) processes could explain the larger variability in altimeter-derived results. Moreover, the fact that peak amplitudes are more often observed in July/August instead of in September (Figure 3c) is likely related to water properties. While the (landfast) ice cover reaches its minimum in September, average water temperature is highest and salinity is lowest in August (Steele et al., 2001).

Differences between altimeter- and model-derived seasonal modulation could also indicate shortcomings of the study/model. First, model simulations are based on landfast ice cover variations of two distinct years, while the altimeter-derived seasonal modulation is calculated based on the entire water level data set (2010–2019). This means that in the altimeter-derived seasonal modulation, interannual variation is averaged out. However, since model simulations are based on two years representing the maximum and minimum landfast ice cover within the time span of the data, the altimeter-derived seasonal modulation is expected to fall within the range of simulated modulation. Nevertheless, judging by the differences between the simulations for 2013 and 2017 (Figures 5e and 5f), the effect of interannual variations in landfast ice cover is small in most of the domain. In regions where the effect of interannual variation is significant (e.g., Hudson Bay), this does not explain the deviation with respect to altimeter-derived modulation. Second, in many Arctic regions, the bathymetry is still largely uncertain, while in some regions the bathymetry has a large impact on tide modeling. This might be of particular importance in Hudson Bay and Hudson Strait which display near-resonant properties (Arbic et al., 2007).

The results presented in this paper indicate that the seasonal modulation of the Arctic M_2 tide can be significant (~20% of amplitude), in particular on shelves and in bays. Our work suggests that, to a large extent, this modification of the tide can be attributed to variations in landfast ice cover. The part that cannot be explained by landfast ice cover variations alone, suggests more research is needed into the impact of other seasonal processes. This entails extending the model approach by including drifting sea ice and updating the bathymetry after the newest GEBCO release, that includes the most recent IBCAO v4 data set on the Arctic (GEBCO Compilation Group, 2020). Finally, while the Arctic sea ice cover varies seasonally, it is also subject to significant inter-annual variability and a declining trend (e.g., Kwok, 2018; Perovich & Richter-Menge, 2009; Serreze & Stroeve, 2015). In our study, the effect of landfast ice on tides was simulated for two years with maximum and minimum cover since 2011. Although differences in ice cover between these years are largest in the Canadian archipelago and on the Russian shelf, the difference in landfast ice cover also alters seasonal modulation of M_2 amplitudes in Hudson and Baffin Bay by up to 0.05 m. This, and the magnitude of the observed relation between seasonal variation in ice extent and tide modification, raises questions concerning the impact of a continuous Arctic sea ice decline. In the particular, since, we showed that the effects of sea ice on tides are not restricted to the Arctic, this calls for further research involving extended use of altimetry data.

5. Summary and Conclusion

The seasonal modulation of the M_2 amplitude and phase, averaged over the period 2010–2019, was obtained for most of the Arctic based on SAR derived water levels from two high-inclination satellite missions, CryoSat-2 and Sentinel-3. Results show significant variations in tidal amplitude (up to 0.25 m) along the Russian coastline, in the Hudson Bay system, the Canadian archipelago and Bering Sea. Phase differences of ~10° are observed throughout the domain, with largest differences along the Russian and Canadian coast (up to 45°).

In addition, the M_2 amplitudes and phases were reproduced for March and September, months with, respectively, the maximum and minimum extent of Arctic landfast ice. Although an amplitude decrease was observed at most locations where landfast ice is present in March (e.g., the Russian coastline, Canadian archipelago, south of Hudson Bay), in other regions (Hudson Strait and Baffin Bay) the amplitude increased. This indicates that landfast ice not only causes local tidal dampening but has an additional far-field effect on tides. These results were subsequently compared to model simulations run for two limiting cases of Arctic landfast ice cover: 1) annually maximum landfast ice cover (March) and 2) no landfast ice cover (September). In many regions model-derived amplitude and phase differences correspond well to the values that were obtained from altimetry. However, in certain regions the positive differences in amplitude (larger in March than in September) are not well captured by the model and simulated phase differences are smaller than observed. Further research is required to fully explain the observed seasonal modulation of the M_2 tide, where other potential drivers besides variations in Arctic landfast ice should be considered.

Finally, the impact of variations in Arctic landfast ice on global tides was assessed by comparing simulated March and September amplitudes to amplitudes derived from tide gauge records. Modeled amplitude differences are considerable (up to 0.05 m) and correspond to the observed signal in several regions, but deviate in other regions. This preliminary analysis emphasizes the importance of further research in the relation between seasonal variations in sea ice and (global) modification of tides.

Data Availability Statement

The Delft3D Flexible Mesh software can be obtained from Deltares (https://oss.deltares.nl/web/delft3d-fm). The instantaneous water levels derived from CryoSat-2 and Sentinel-3 are deposited online (https://doi.org/10.4121/13084493) and computed tidal constants can be found here: https://doi.org/10.4121/uuid:1d027d6a-e8a7-4910-8358-46b174f256fe.

References

Arbic, B. K., & Garrett, C. (2010). A coupled oscillator model of shelf and ocean tides. *Continental Shelf Research*, *30*(6), 564–574. https://doi.org/10.1016/j.csr.2009.07.008

Arbic, B. K., MacAyeal, D. R., Mitrovica, J. X., & Milne, G. A. (2004). Ocean tides and Heinrich events. *Nature*, *432*(7016). 460. https://doi.org/10.1038/432460a

Arbic, B. K., St-Laurent, P., Sutherland, G., & Garrett, C. (2007). On the resonance and influence of the tides in Ungava Bay and Hudson Strait. *Geophysical Research Letters*, *34*(17). https://doi.org/10.1029/2007gl030845

Caldwell, P. C., Merrifield, M. A., & Thompson, P. R. (2015). *Sea level measured by tide gauges from global oceans—the Joint Archive for Sea Level holdings (NCEI Accession 0019568) Version 5.5*. NOAA National Centers for Environmental Information, Dataset. Retrieved from https://doi.org/10.7289/V5V40S7W

Cancet, M., Andersen, O. B., Lyard, F., Cotton, D., & Benveniste, J. (2018). Arctide2017, a high-resolution regional tidal model in the Arctic Ocean. *Advances in Space Research*, *62*(6), 1324–1343. https://doi.org/10.1016/j.asr.2018.01.007

Codiga, D. (2020). *UTide unified tidal analysis and prediction functions*. MATLAB Central File Exchange. Retrieved from https://www.mathworks.com/matlabcentral/fileexchange/46523-utide-unified-tidal-analysis-and-prediction-functions

Dinardo, S., Fenoglio-Marc, L., Buchhaupt, C., Becker, M., Scharroo, R., Fernandes, M. J., & Benveniste, J. (2018). Coastal and PLRM altimetry in German Bight and West Baltic Sea. *Advances in Space Research*, *6*(2), 1371–1404. https://doi.org/10.1016/j.asr.2017.12.018

Donlon, C., Berruti, B., Buongiorno, A., Ferreira, M.-H., Féménias, P., Frerick, J., et al. (2012). The global monitoring for environment and security (GMES) sentinel-3 mission. *Remote Sensing of Environment*, *120*, 37–57. https://doi.org/10.1016/j.rse.2011.07.024

Foreman, M. G. G., & Henry, R. F. (1989). The harmonic analysis of tidal model time series. *Advances in Water Resources*, *12*(3), 109–120. https://doi.org/10.1016/0309-1708(89)90017-1

GEBCO Compilation Group (2019). *Gebco 2029 grid*. Retrieved from https://doi.org/10.5285/836f016a-33be-6ddc-e053-6c86abc0788e

GEBCO Compilation Group (2020). *Gebco 2020 grid*. Retrieved from https://doi.org/10.5285/a29c5465-b138-234d-e053-6c86abc040b9

Godin, G. (1986). Modification by an ice cover of the tide in James Bay and Hudson Bay. *Arctic*, *39*(1), 65–67. https://doi.org/10.14430/arctic2048

Hibler, W. D. (1979). A dynamic thermodynamic sea ice model. *Journal of Physical Oceanography*, *9*(4), 815–846. https://doi.org/10.1175/1520-0485(1979)009<0815:adtsim>2.0.co;2

Hibler, W. D., Roberts, A., Heil, P., Proshutinsky, A. Y., Simmons, H. L., & Lovick, J. (2006). Modeling M2 tidal variability in Arctic sea-ice drift and deformation. *Annals of Glaciology*, *44*, 418–428. https://doi.org/10.3189/172756406781811178

Jain, M., Martin-Puig, C., Andersen, O. B., Stenseng, L., & Dall, J. (2014). Evaluation of SAMOSA3 adapted retracker using CryoSat-2 SAR altimetry data over the Arctic ocean. Paper presented at *IEEE Geoscience and Remote Sensing Symposium*, (pp. 5115–5118). IEEE.

Kagan, B. A., & Romanenkov, D. A. (2007). On the variability of tidal constants induced by the influence of one subsystem on another. *Izvestiya: Atmospheric and Oceanic Physics*, *43*(3), 357–362. https://doi.org/10.1134/s0001433807030103

Kagan, B. A., Romanenkov, D. A., & Sofina, E. V. (2007). Modeling the tidal ice drift and ice-induced changes in tidal dynamics on the Siberian continental shelf. *Izvestiya: Atmospheric and Oceanic Physics*, *43*(6), 766–784. https://doi.org/10.1134/S0001433807060114

Kagan, B. A., & Sofina, E. V. (2010). Ice-induced seasonal variability of tidal constants in the Arctic Ocean. *Continental Shelf Research*, *30*(6), 643–647. https://doi.org/10.1016/j.csr.2009.05.010

Kleptsova, O., & Pietrzak, J. D. (2018). High resolution tidal model of Canadian Arctic Archipelago, Baffin and Hudson Bay. *Ocean Modelling*, *128*, 15–47. https://doi.org/10.1016/j.ocemod.2018.06.001

Kowalik, Z. (1981). A Study of the M-2 Tide in the ice-covered Arctic Ocean. *Modeling, Identification and Control*, *2*(4), 201–223. https://doi.org/10.4173/mic.1981.4.2

Kulikov, M. E., Medvedev, I. P., & Kondrin, A. T. (2018). Seasonal variability of tides in the Arctic Seas. *Russian Journal of Earth Sciences*, *18*(5). https://doi.org/10.2205/2018ES000633

Kwok, R. (2018). Arctic sea ice thickness, volume, and multiyear ice coverage: Losses and coupled variability (19582018). *Environmental Research Letters*, *13*(10), 105005. https://doi.org/10.1088/1748-9326/aae3ec

Langleben, M. P. (1982). Water drag coefficient of first-year sea ice. *Journal of Geophysical Research*, *87*(C1), 573. https://doi.org/10.1029/jc087ic01p00573

Laxon, S. (1994). Sea ice altimeter processing scheme at the EODC. *International Journal of Remote Sensing*, *15*(4), 915–924. https://doi.org/10.1080/01431169408954124

Li, Z., Zhao, J., Su, J., Li, C., Cheng, B., Hui, F., et al. (2020). Spatial and temporal variations in the extent and thickness of arctic landfast ice. *Remote Sensing*, *12*(1), 64. https://doi.org/10.3390/RS12010064

Müller, M., Cherniawsky, J. Y., Foreman, M. G. G., & von Storch, J.-S. (2014). Seasonal variation of the M 2 tide. *Ocean Dynamics*, *64*(2), 159–177. https://doi.org/10.1007/s10236-013-0679-0

Madsen, O. S., & Bruno, M. S. (1987). A methodology for the determination of drag coefficients for ice floes. *Journal of Offshore Mechanics and Arctic Engineering*, *109*(4), 381–387. https://doi.org/10.1115/1.3257035

Mahoney, A. R., Eicken, H., Gaylord, A. G., & Gens, R. (2014). Landfast sea ice extent in the Chukchi and Beaufort Seas: The annual cycle and decadal variability. *Cold Regions Science and Technology*, *103*, 41–56. https://doi.org/10.1016/j.coldregions.2014.03.003

McPhee, M. G. (1980). An analysis of pack ice drif in summer. In R. Pritchard (Ed.), *Sea-ice processes and models* (pp. 62–75). Seatle, WA: University of Washington Press.

Müller, M. (2012). The influence of changing stratification conditions on barotropic tidal transport and its implications for seasonal and secular changes of tides. *Continental Shelf Research*, *47*, 107–118. https://doi.org/10.1016/j.csr.2012.07.003

Müller, M., Cherniawsky, J. Y., Foreman, M. G. G., & von Storch, J. S. (2012). Global M2 internal tide and its seasonal variability from high resolution ocean circulation and tide modeling. *Geophysical Research Letters*, *39*(19). https://doi.org/10.1029/2012gl053320

National Snow and Ice Data Center (2020). *Charctic interactive sea ice graph*. Retrieved from https://nsidc.org/arcticseaicenews/charctic-interactive-sea-ice-graph/

Pawlowicz, R., Beardsley, B., & Lentz, S. (2002). Classical tidal harmonic analysis including error estimates in MATLAB using T_TIDE. *Computers & Geosciences*, *28*, 929–937. https://doi.org/10.1016/s0098-3004(02)00013-4

Pease, C. H., Salo, S. A., & Overland, J. E. (1983). Drag measurements for first-year sea ice over a shallow sea. *Journal of Geophysical Research*, *88*(C5), 2853. https://doi.org/10.1029/JC088iC05p02853

Perovich, D. K., & Richter-Menge, J. A. (2009). Loss of sea ice in the Arctic. *Annual Review of Marine Science*, *1*, 417–441. https://doi.org/10.1146/annurev.marine.010908.163805

Pickering, M. D., Horsburgh, K. J., Blundell, J. R., Hirschi, J. J.-M., Nicholls, R. J., Verlaan, M., & Wells, N. C. (2017). The impact of future sea-level rise on the global tides. *Continental Shelf Research*, *142*, 50–68. https://doi.org/10.1016/j.csr.2017.02.004

Poisson, J.-C., Quartly, G. D., Kurekin, A. A., Thibaut, P., Hoang, D., & Nencioli, F. (2018). Development of an ENVISAT altimetry processor providing sea level continuity between open ocean and Arctic leads. *IEEE Transactions on Geoscience and Remote Sensing*, *56*(9), 5299–5319. https://doi.org/10.1109/tgrs.2018.2813061

Prinsenberg, S. J., & Freeman, N. G. (1986). Chapter 11 tidal heights and currents in Hudson Bay and James Bay. In I. P. Martini (Ed.), *Canadian inland seas* (pp. 205–216). Amsterdam: Elsevier. https://doi.org/10.1016/s0422-9894(08)70904-8

Ray, C., Martin-Puig, C., Clarizia, M. P., Ruffini, G., Dinardo, S., Gommenginger, C., & Benveniste, J. (2015). SAR altimeter backscattered waveform model. *IEEE Transactions on Geoscience and Remote Sensing*, *53*(2), 911–919. https://doi.org/10.1109/tgrs.2014.2330423

Savcenko, R., & Bosch, W. (2007). Residual Tide Analysis in Shallow Water - Contributions of ENVISAT and ERS Altimetry. In *Envisat symposium*.

Schulz, A.-T., & Naeije, M. (2018). Sar retracking in the arctic: Development of a year-round retrackers system. *Advances in Space Research*, *62*(6), 1292–1306. https://doi.org/10.1016/j.asr.2018.01.037

Serreze, M. C., & Stroeve, J. (2015). Arctic sea ice trends, variability and implications for seasonal ice forecasting. *Philosophical Transactions of the Royal Society A: Mathematical, Physical & Engineering Sciences*, *373*. https://doi.org/10.1098/rsta.2014.0159

Steele, M., Morley, R., & Ermold, W. (2001). PHC: A global ocean hydrography with a high-quality Arctic Ocean. *Journal of Climate*, *14*(9), 2079–2087. https://doi.org/10.1175/1520-0442(2001)014<2079:pagohw>2.0.co;2

St-Laurent, P., Saucier, F. J., & Dumais, J. F. (2008). On the modification of tides in a seasonally ice-covered sea. *Journal of Geophysical Research*, *113*(11), 1–11. https://doi.org/10.1029/2007JC004614

Sverdrup, H. (1927). Dynamics of tides on the north Siberian Shelf. *Geofysiske Publikasjoner*, *4*, 3–75.

U.S. National Ice Center. (2009). *National ice center Arctic sea ice charts and climatologies in gridded format Version 1*. Boulder, CO: NSIDC: National Snow and Ice Data Center. Retrieved from https://doi.org/10.7265/N5X34VDB

Verlaan, M., De Kleermaeker, S., & Buckman, L. (2015). GLOSSIS: Global storm surge forecasting and information system. Paper presented at *Australian Coasts and Ports 2015 Conference(September)* (pp. 229–234). Engineers Australia and IPENZ.

Wang, X., Verlaan, M., Apecechea, M. I., & Lin, H. X. (2021). Computation efficient parameter estimation for a high resolution global tide and surge model (GTSM). *Journal of Geophysical Research: Oceans*, *126*, e2020JC016917. https://doi.org/10.1029/2020JC016917

Wernecke, A., & Kaleschke, L. (2015). Lead detection in arctic sea ice from cryosat-2: Quality assessment, lead area fraction and width distribution. *The Cryosphere*, *9*(5), 1955–1968. https://doi.org/10.5194/tc-9-1955-2015

Wingham, D. J., Francis, C. R., Baker, S., Bouzinac, C., Brockley, D., Cullen, R., et al. (2006). CryoSat: A mission to determine the fluctuations in Earth's land and marine ice fields. *Advances in Space Research*, *37*(4), 841–871. https://doi.org/10.1016/j.asr.2005.07.027

Zijl, F., Verlaan, M., & Gerritsen, H. (2013). Improved water-level forecasting for the Northwest European Shelf and North Sea through direct modelling of tide, surge and non-linear interaction. *Ocean Dynamics*, *63*(7), 823–847. https://doi.org/10.1007/s10236-013-0624-2

Zijl, F., Verlaan, M., & Irazoqui, M. (2016). *On the origins of annual modulation of M2 and M4 harmonic consituents*. Retrieved from https://publicwiki.deltares.nl/download/attachments/122847685/JONSMOD2016_Presentation_1-7_Zijl.pdf?version=1&modificationDate=1463494525000&api=v2

References From the Supporting Information

Kowalik, Z., & Proshutinsky, A. Y. (1994). The Arctic ocean tides. In: In O. M. Johannessen, R. D. Muench, & J. E. Overland (Eds.), *The polar oceans and their role in shaping the global environment, Geophysical Monograph* (Vol. *85*, pp. 137-158). Washington, DC: American Geophysical Union.

Stammer, D., Ray, R. D., Andersen, O. B., Arbic, B. K., Bosch, W., Carrère, L., et al. (2014). Accuracy assessment of global barotropic ocean tide models. *Reviews of Geophysics*, *52*(3), 243–282.

Erratum

In the originally published version of this article, the x-ticks of Figure 6d and 6e were incorrectly labeled. This error has been corrected, and this may be considered the official version of record.